Journal of Computational Physics **149,** 389–417 (1999)
Article ID jcph.1998.6161, available online at http://www.idealibrary.com on IDEAL®

Using a Curvilinear Grid to Construct Symmetry-Preserving Discretizations for Lagrangian Gas Dynamics

Len Margolin* and Mikhail Shashkov†

*Los Alamos National Laboratory, *X-HM, MS-D413, †T-7, MS-B284, Los Alamos, New Mexico 87545*
E-mail: †shashkov@lanl.gov

Received August 20, 1998; revised November 20, 1998

The goal of this paper is to construct discretizations for the equations of Lagrangian gas dynamics that preserve plane, cylindrical, and spherical symmetry in the solution of the original differential equations. The new method uses a curvilinear grid that is reconstructed from a given logically rectangular distribution of nodes. The sides of the cells of the reconstructed grid can be segments of straight lines or arcs of local circles. Our procedure is exact for straight lines and circles; that is, it reproduces rectangular and polar grids exactly. We use the method of support operators to construct a conservative finite-difference method that we demonstrate will preserve spatial symmetries for certain choices of the initial grid. We also introduce a "curvilinear" version of artificial edge viscosity that also preserves symmetry. We present numerical examples to demonstrate our theoretical considerations and the robustness of the new method.

Key Words: curvilinear grids; grid reconstruction; invariant discretizations; preservation of symmetry.

1. INTRODUCTION

The purpose of this paper is to demonstrate the feasibility of preserving certain physical symmetries in numerical simulations of fluid flow by using higher-order reconstructions of the computational grid. In a typical two-dimensional Lagrangian calculation, the nodes move each cycle with the local fluid velocity, and then the mesh is reconstructed by connecting neighboring nodes with straight lines. Our strategy here will be to use higher-order curves to connect the nodes, so that planar, cylindrical, and spherical symmetries will be exactly maintained, while the simulation of other symmetries will be enhanced. While demonstrating feasibility, we recognize that our particular algorithm is derived heuristically, and that further research may lead to significant improvements. Nevertheless, we believe that the utility of more general grids is in itself worth illustrating.

0021-9991/99 $30.00

The importance of preserving physical symmetries in Lagrangian simulation is well recognized. For example, the preservation of spherical symmetry in numerical simulations of implosion is critically important in the inertial confinement fusion (ICF) program [12, 39, 37]. There small departures from spherical symmetry due to discrete errors may be amplified by Rayleigh–Taylor instability [1, 13, 14], leading to unacceptably large errors in problems with strong compressions. Also, uncertainty as to whether a nonsymmetric result is due to numerical errors or to the physical design inhibits our understanding of the dynamics of the implosion and so severely limits our predictive capabilities.

Previous work has concentrated on the form of the difference approximations rather than on the grid. In fact, both the choice of the discrete operators and the method of grid reconstruction can lead to the loss of symmetry in calculations. Once a grid has been chosen, it is necessary to construct approximations to spatial operators like divergence, gradient, and curl. We shall show that the method of support operators provides a general framework for constructing these operators, once the grid is determined. Furthermore the method of support operators leads to conservative finite-difference methods.

Reviewing previous work, we can distinguish between those methods that preserve symmetry exactly and those that improve the preservation of symmetry. The straightforward approach to preserving symmetry exactly on a polar grid is to use spherical coordinates as the primary coordinates and the corresponding components of velocity field in the discrete model [34, 37]. This approach is expensive because it is requires the computation of trigonometric functions. Moreover, because these methods use the equations of gas dynamics in spherical coordinates, special care has to be taken in discretizing terms containing $1/R$, which appear due to the dependence of the basis vectors on position. Also the use of spherical coordinates is not accurate for systems evolving far from sphericity.

In practice, the most widely used methods that preserve symmetry exactly on polar grids with equiangular zoning are the "area-weighted" methods [2, 38, 35]. In this approach, one uses a Cartesian form of the momentum equation in a cylindrical coordinate system. The term "area-weighted" originates when this approach is used in the framework of finite-element methods, where integration is not performed with respect to the true volume in cylindrical coordinates, but rather with respect to area. A drawback of this approach is that it works only for the equiangular grid. In practice, one finds large errors when the angular zoning is not uniform, especially near the symmetry axes. For a general discussion, see [3]. In this reference, a generalization termed the modified gradient method [3] is described in which the forces are modified locally according to the expected symmetry of the flow.

An alternate strategy does not seek to preserve symmetry exactly, but rather to improve the representation of symmetry over more standard methods. One such strategy is termed the "mass matrix" approach [25–27]. A standard technique in finite volume algorithms is to calculate the acceleration as the surface integral of the pressure gradient over a "momentum control" volume. The acceleration so calculated should be applied to the center of mass of this volume, which usually does not coincide with the node point. In the "mass matrix" approach, one distinguishes between the center of mass and the node point and attempts to compensate for the difference. This can be accomplished explicitly, by correcting the acceleration of the node using the accelerations at some neighboring nodes, or implicitly, by introducing the mass matrix and solving a system of linear equations.

Another approach to improve symmetry is based on using a nonconservative form of the governing equations [33]. There it is shown that a nonconservative form can yield a

considerable improvement in symmetry when compared with methods based on a conservative form.

Still another approach to constructing Eulerian methods [24, 23] with improved symmetry on uniform grids is based on analyzing the group symmetry properties of the modified equations [40]. There are also theoretical papers such as [10], where group properties are investigated in more detail.

All the methods described above use traditional grids, in which the nodes are connected by segments of straight lines. One obvious disadvantage of using such grids is that for domains with curvilinear boundaries, additional errors are introduced that are related to the approximation of the boundary. For example, in problems with spherical symmetry the domain of the original differential equations is a sphere, but the computational domain is a polygon. Also, for such an approximation of the boundary it is not clear how to specify the boundary conditions; from the statement of the original problem we know boundary conditions only on the curvilinear boundary but not on the boundary of the polygon. In the context of the equations of Lagrangian gas dynamics, the same uncertainty applies to interfaces between different materials. For methods that use a staggered data structure, there is also a problem in specifying the initial conditions because thermodynamic quantities, like pressure, are assigned to the entire "cell" and one has to specify these values. The simplest choice, which is used in practice, is to compute the value at the "geometric center" of the cell. However, for general polar grids, the radii of these cell centers are not equal.

There is at least one (to our knowledge) approach to solve the equations of gas dynamics in mixed Eulerian–Lagrangian form, where a method of the Godunov type is used on moving *curvilinear* grids [15, 32]. This algorithm preserves some spatial symmetries exactly, but does not appear applicable to finite difference codes.

It is well known from the finite-element method (FEM) literature [8, 16, 41, 42] that introducing curvilinear grids for domains with curvilinear boundaries increases the accuracy of simulation. The improvement in accuracy results from the simple fact that one can approximate a given boundary more accurately using high-order splines than with segments of straight lines. In this paper we employ curvilinear grids throughout the domain and construct our difference approximations consistently to achieve a different goal, namely the preservation of the physical symmetry of the solution.

The paper is organized as follows. In Section 2 we describe an algorithm for reconstructing the curvilinear grid and then give examples of reconstructed grids. In Section 3 we define a notation for various elements of the curvilinear grid, and also describe the spaces of grid functions. In Section 4 we derive discrete analogs of the divergence and gradient operators on the curvilinear grid and prove their symmetry properties. In Section 5 we use these operators to construct a finite difference algorithm for Lagrangian gas dynamics. In Section 6 we define the notion of spatial symmetries for the discrete model and prove that our algorithms preserve these symmetries. In Section 7 we further prove that the corresponding algorithm, implemented on the grid with straight lines, does not preserve spherical symmetry. In Section 8 we present numerical examples, which verify our analysis and illustrate the robustness of the algorithm.

To make this paper self-contained, in Appendices A and B we provide the necessary formulas for lengths, areas, and volumes, and describe an edge artificial viscosity for the curvilinear grid that preserves symmetry.

2. GRID RECONSTRUCTION

We consider a logically rectangular distribution of points in two spatial dimensions, representing the nodes of a grid, such that the points can be labeled by two indices, i and j (as in the case of a rectangular grid). For each node $P_{i,j}$ the coordinates are $x_{i,j}$, $y_{i,j}$. When the grid points with fixed i (j) are connected by segments of straight lines, the grid cells are general quadrilaterals. The broken line connecting the points can be thought of as the simplest approximation to some smooth curve that goes through these points.

It is clear that there is no unique way to draw a curve going through these points. In this section we describe an algorithm for the reconstruction of the curve that is exact when the points lie on a straight line or on the circumference of a circle. By exact, we mean that if the points $i = const$ ($j = const$) lie on a straight line or circle, then our method will reconstruct this line or circle. Our algorithm is local, by which we mean that the reconstructed curve between two points is based only on the coordinates of those two points and a few neighboring points.

A further restriction of our algorithm is that we reconstruct the curves independently for each family—that is, when we reconstruct the curve corresponding to fixed i (j) we use only information from neighboring points with the same fixed i (j). More particularly, to reconstruct the curve between two points, we use information only from these points, and the two nearest neighbors in the family. This algorithm is similar to one described in [15].

Our construction is based on a well-known property of central and inscribed angles in a circle. Let us consider four points P_{i-1}, P_i, P_{i+1}, P_{i+2} that lie on the same circle; the index increases as we move clockwise along the circle, see Fig. 1a. We denote the center of the circle by O. We also denote the angle $\angle P_i P_{i-1} P_{i+1}$ by α, the angle $\angle P_{i+1} P_{i+2} P_i$ by β, and the central angle $\angle P_i O P_{i+1}$ by γ. It is known from elementary geometry that all inscribed angles based on the same arc are equal to each other and equal to one-half of the central angle based on the same arc; that is, $\alpha = \beta = \gamma/2$, and therefore $\gamma = \alpha + \beta$.

Now let us consider an arbitrary set of four points, P_{i-1}, P_i, P_{i+1}, P_{i+2}. We will use the coordinates of these points to reconstruct the curve between the points P_i, P_{i+1} as a piece of

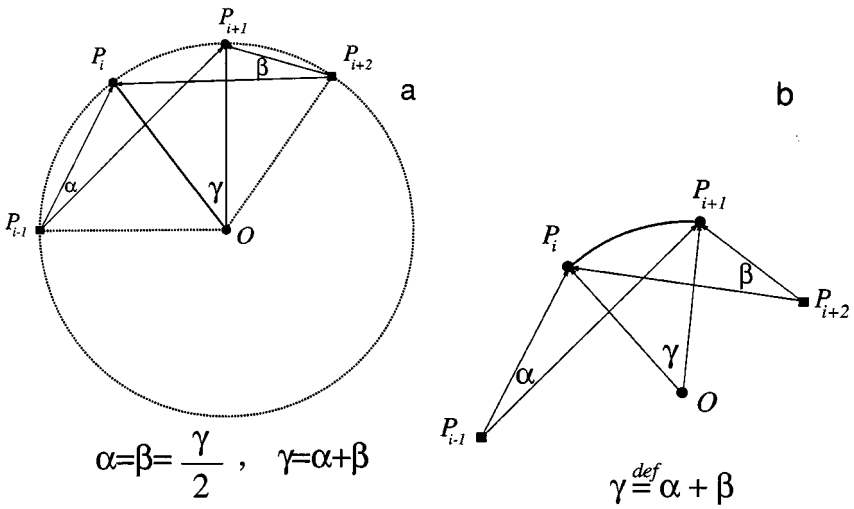

FIG. 1. (a) Illustration of the relation of the central and inscribed angles of a circle, (b) reconstruction of the local circle.

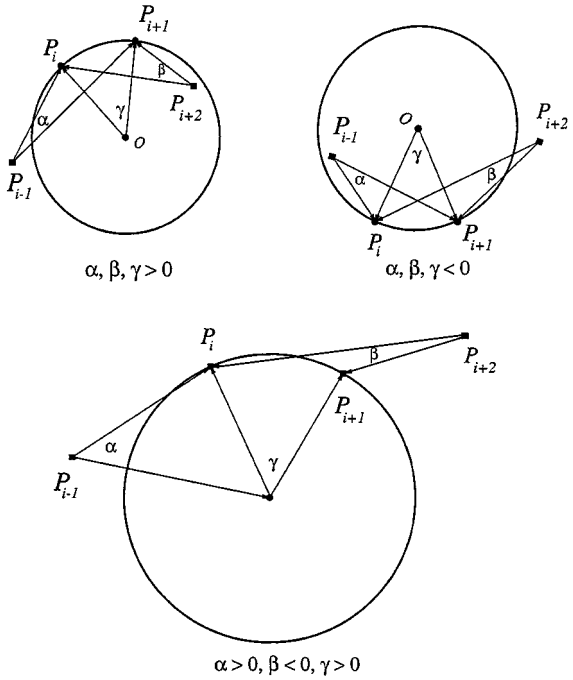

FIG. 2. Different cases of the reconstruction of the local circle.

a circle. This circle has to pass through these two points, which gives us two conditions. To define a unique circle we specify the central angle γ. In the case of an arbitrarily positioned set of four points, we compute the angles $\alpha = \angle P_i P_{i-1} P_{i+1}$ and $\beta = \angle P_i P_{i+2} P_{i+1}$, and then define

$$\gamma \stackrel{\text{def}}{=} \alpha + \beta.$$

For the angle α, we consider the direction from segment $P_{i-1}P_{i+1}$ to segment $P_{i-1}P_i$ as the positive direction. Therefore the angle α will vary from $-\pi$ to π. A similar convention is adopted for the angle β, where the positive direction is from $P_{i+2}P_i$ to $P_{i+2}P_{i+1}$. The situation where both angles, α and β are positive is shown in Fig. 1b. Finally, we define the curve between points P_i, P_{i+1} as the arc of the circle that goes through these points and has the central angle γ. This procedure is illustrated in Fig. 1b. We note that the angles α and β can become negative when the orientation of the points is changed. This means that the angle γ also can be negative or zero. That γ is negative indicates a different orientation of arc $P_i P_{i+1}$ with respect to the local polar coordinate system (see Fig. 2).

In Fig. 2 we show several different possible situations: (a) the situation where all α, β, and $\gamma > 0$; (b) the situation where all α, β, and $\gamma < 0$; (c) the situation where all $\alpha > 0$, $\beta < 0$, but $|\alpha| > |\beta|$, that is, $\gamma > 0$.

When $\gamma = 0$ we reconstruct the curve between points $P_i P_{i+1}$ as a segment of a straight line. As a matter of implementation, we connect two points by a straight line whenever $|\gamma| < 10^{-12}$. It is clear that this algorithm will be exact whenever the four points lie on a straight line, or on the circumference of a circle.

We illustrate our algorithm by presenting examples of grid reconstruction for three logically rectangular distributions of nodes. First, in Fig. 3a we present the usual grid, where the

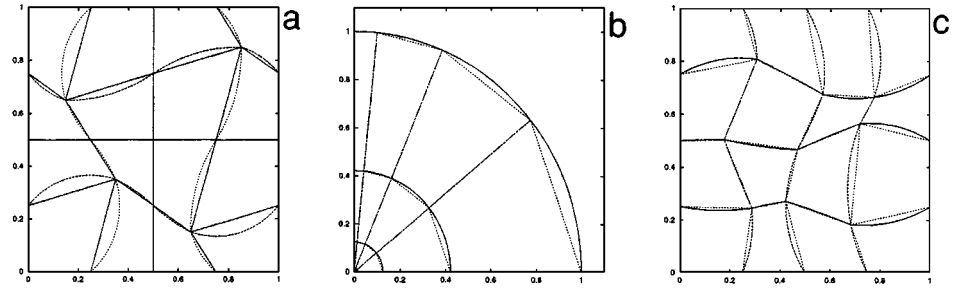

FIG. 3. Smooth logically rectangular distribution of nodes, $M = N = 5$. (a) Comparison of the usual grid (nodes connected by segments of straight lines) and the piecewise smooth reconstruction (nodes connected by arcs of the circles). (b) Polar distribution of nodes. Grid nonuniform in angle and in radius. (c) Random logically rectangular distribution of nodes.

nodes are connected by segments of straight lines, superimposed on our new reconstruction using piecewise circles, for points in $(x, y) \in [0:1] \times [0:1]$, obtained by mapping

$$x(\xi, \eta) = \xi + 0.1 * \sin(2\pi\xi) * \sin(2\pi\eta), \qquad y(\xi, \eta) = \eta + 0.1 * \sin(2\pi\xi) * \sin(2\pi\eta),$$

from a uniform grid ($M = N = 5$) in the unit square in $(\xi, \eta) \in [0:1] \times [0:1]$. Second, in Fig. 3b we present the grids for a polar distribution of nodes—i.e., the coordinates of the nodes are

$$x_{i,j} = R_j \sin\theta_i, \qquad y_{i,j} = R_j \cos\theta_i,$$

where the angle θ equals 0 at the y axis and increases as the angle rotates toward the x axis. In this case the grid consists of perfect circles and straight lines, whether or not the angular zones have equal width.

Finally we consider a nonsmooth logically rectangular grid distribution. This distribution is obtained from a uniform grid by random displacement of each point from its original position within the limits of a small square whose center is the original position of the point. The resulting grids are shown in Fig. 3c.

To construct our discretizations, we will need to compute the lengths, areas, and volumes for the new curvilinear grid. We distinguish between two different cases. In the first case, we consider 2-D figures in the $x - y$ plane. For these figures we need formulas for the lengths of the curved sides of a cell and for the areas of the enclosed quadrilateral. These quantities will be used in the case of 2-D finite-difference schemes in Cartesian geometry. In the second case we consider 3-D figures, which are obtained by the revolution of our 2-D figures around an axis of symmetry. Here we think of the $x - y$ axes as the $r - z$ axes of a cylindrical coordinate system. Such figures are used in the calculation of problems with cylindrical symmetry. For these figures we need the formulas for the areas of surfaces obtained by revolution of the curved sides (i.e., the faces of the 3-D cell) and for the volume of the 3-D figure of revolution. In this case all quantities are normalized to 2π. The lengths of the edges, the areas of the faces, and the volumes of the cells all can be computed exactly. In Appendix A we provide the necessary formulas.

For simplicity, throughout this paper we will refer to the geometric elements in the $x - y$ case as if they belong to $r - z$ case.

3. ELEMENTS OF THE CURVILINEAR GRID

In this section we describe our notation for the elements of the curvilinear grid that we have constructed in the previous section. We will also introduce some additional geometrical objects.

The nodes of the grid are denoted by the pair of indices (i, j). The midpoints of the sides—i.e., the points that divide the edges into two pieces with equal lengths—are denoted by one integer index and one half-integer index: $(i + 1/2, j)$ or $(i, j + 1/2)$. For the sides themselves, we use the same indices as the midpoints. The midpoint divides the side into two subsides. These subsides have superscripts that coincide with the index of the corresponding side and subscripts that indicate which vertex is an endpoint. For example, the area corresponding to the subside of the side connecting nodes (i, j) and $(i, j + 1)$ and having node (i, j) as an endpoint is denoted by $S\xi_{i,j}^{i,j+1/2}$. We could write $S_{i,j}^{i,j+1/2}$ instead of $S\xi_{i,j}^{i,j+1/2}$, but we prefer the latter notation because it is then clearer to which side we refer. Notations for the other areas are shown in Fig. 4.

Next, we introduce the "median" grid. The edges of the median grid pass through the midpoints of the edges of the primary grid, and are constructed in exactly the same manner—i.e., they can be arcs of circles or segments of straight lines, see Fig. 4. The intersection of the edges of the median grid within a cell defines a point in the cell, which we call the "cell center," denoted by the indices $(i + 1/2, j + 1/2)$. Also these two edges subdivide the cell into four subcells. To designate these subcells, we again use both superscripts and subscripts. The superscripts correspond to the index of the cell, while the subscripts correspond to the index of the point that is a vertex of the original grid, which is also a vertex of the subcell. The volume enclosed by the four subcells surrounding a node is sometimes termed the "momentum control volume."

For each side we can define two unit normal vectors; these are the normals to the circle at the nodes (i.e., the endpoints of the arc). Note that when the side is a segment of a straight line, the normal vectors are parallel. The designation for these normals is the same as for subsides, Fig. 4. Note that there will be four unit normal vectors at each node, Fig. 5.

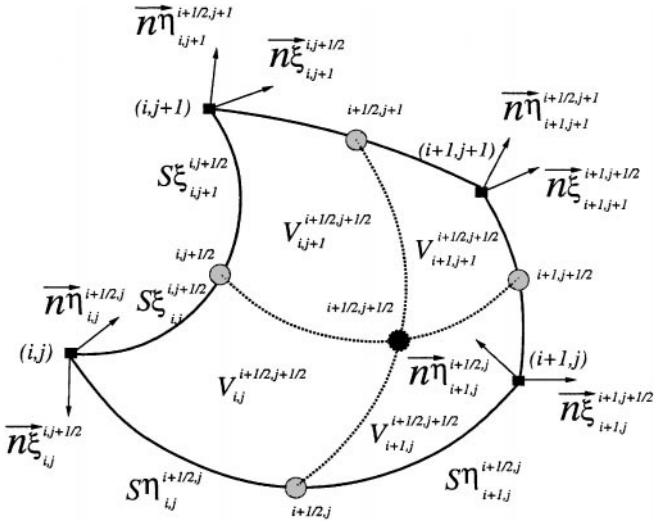

FIG. 4. Notations for the areas of faces and volumes.

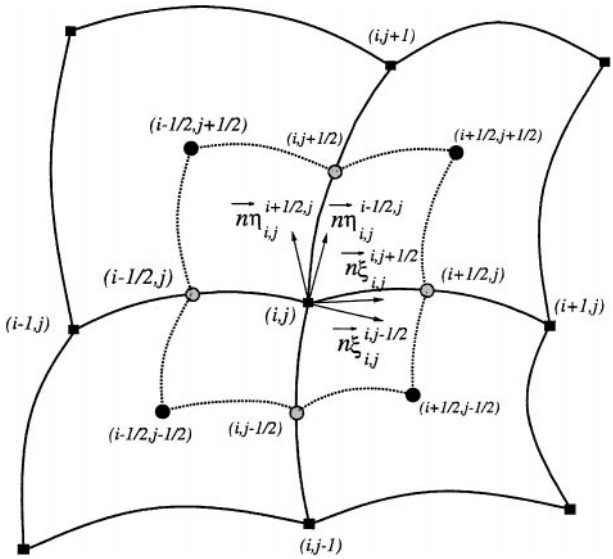

FIG. 5. Notation related to the momentum control volume.

4. DISCRETE OPERATORS ON CURVILINEAR GRIDS

In this section we construct the discrete analogs of the differential operators **div** and **grad** on the curvilinear grid. These will be used to construct the finite difference algorithm for the equations of Lagrangian gas dynamics.

We assume a data structure that is the standard for staggered grid. Here thermodynamic variables such as pressure, p, which are scalar grid functions, are defined at the cell centers. We denote the space of such discrete scalar functions as HC. Both components of vector fields, such as velocity $\vec{U}$, are defined at the nodes of the original grid. We denote the space of such discrete vector functions as $\mathcal{HN}$.

We define the discrete analog of the operator **div** in a coordinate invariant form

$$\mathbf{div}\,\vec{W} = \lim_{V\to 0} \frac{\oint_{\partial V} (\vec{W},\vec{n})\,dS}{V}. \tag{4.1}$$

We choose the computational cell of the original grid as the volume of integration, V. Then the domain and range of our discrete divergence are $\mathbf{DIV} : \mathcal{HN} \to HC$.

We represent the boundary integral in (4.1) as the sum of boundary integrals over the individual faces and then subdivide each arc into two subarcs. The boundary integral over each subarc is approximated by the value of the dot product $(\vec{W},\vec{n})$, evaluated at the corresponding vertex of the original grid, and then multiplied by the area of the subarc. The resulting formula is

$$\begin{aligned}
&(\mathbf{DIV}\,\vec{W})_{i+1/2,\,j+1/2} \\
&\quad = \Big\{\Big[\big((\vec{W}_{i+1,j}, \vec{n\xi}^{\,i+1,j+1/2}_{i+1,j})\,S\xi^{i+1,j+1/2}_{i+1,j} + (\vec{W}_{i+1,j+1}, \vec{n\xi}^{\,i+1,j+1/2}_{i+1,j+1})\,S\xi^{i+1,j+1/2}_{i+1,j+1}\big) \\
&\qquad - \big((\vec{W}_{i,j}, \vec{n\xi}^{\,i,j+1/2}_{i,j})\,S\xi^{i,j+1/2}_{i,j} + (\vec{W}_{i,j+1}, \vec{n\xi}^{\,i,j+1/2}_{i,j+1})\,S\xi^{i,j+1/2}_{i,j+1}\big)\Big] \\
&\qquad + \Big[\big((\vec{W}_{i,j+1}, \vec{n\eta}^{\,i+1/2,j+1}_{i,j+1})\,S\eta^{i+1/2,j+1}_{i,j+1} + (\vec{W}_{i+1,j+1}, \vec{n\eta}^{\,i+1/2,j+1}_{i+1,j+1})\,S\eta^{i+1/2,j+1}_{i+1,j+1}\big) \\
&\qquad - \big((\vec{W}_{i,j}, \vec{n\eta}^{\,i+1/2,j}_{i,j})\,S\eta^{i+1/2,j}_{i,j} + (\vec{W}_{i+1,j}, \vec{\eta\eta}^{\,i+1/2,j}_{i+1,j})\,S\eta^{i+1/2,j}_{i+1,j}\big)\Big]\Big\}\big/ V_{i+1/2,\,j+1/2}.
\end{aligned} \tag{4.2}$$

To construct the discrete analog of **grad** we use the support operator method (SOM), [30, 29, 31]. In this methodology the discrete gradient, **GRAD**, is derived from the given discrete divergence, **DIV**, by enforcing a discrete analog of the integral identity

$$\int_V \varphi\, \mathbf{div}\, \vec{W}\, dV + \int_V (\vec{W}, \mathbf{grad}\, \varphi)\, dV = \oint_{\partial V} \varphi(\vec{W}, \vec{n})\, dS, \tag{4.3}$$

which relates **div** and **grad**, where φ and $\vec{W}$ are an arbitrary scalar and a vector function, respectively.

We can without loss of generality neglect the boundary term in (4.3) and write a discrete analog of this integral identity as

$$\sum_{cells} \varphi_{i+1/2,\,j+1/2} (\mathbf{DIV}\, \vec{W})_{i+1/2,\,j+1/2} V_{i+1/2,\,j+1/2} + \sum_{nodes} (\vec{W}, \mathbf{GRAD}\, \varphi)_{i,\,j} V_{i,\,j} = 0, \tag{4.4}$$

where $V_{i,\,j}$ is a volume associated with the node.

$$V_{i,\,j} = V_{i,\,j}^{i+1/2,\,j+1/2} + V_{i,\,j}^{i-1/2,\,j+1/2} + V_{i,\,j}^{i-1/2,\,j-1/2} + V_{i,\,j}^{i+1/2,\,j-1/2}. \tag{4.5}$$

To derive the operator **GRAD** we consider (4.4) as an identity with respect to $\vec{W}$. Then by regrouping terms, we find that

$$\begin{aligned}
(\mathbf{GRAD}\, \varphi)_{i,\,j} = \big\{ & (\varphi_{i+1/2,\,j+1/2} - \varphi_{i+1/2,\,j-1/2}) S\eta_{i,\,j}^{i+1/2,\,j} \vec{n}\eta_{i,\,j}^{i+1/2,\,j} \\
& + (\varphi_{i-1/2,\,j+1/2} - \varphi_{i-1/2,\,j-1/2}) S\eta_{i,\,j}^{i-1/2,\,j} \vec{n}\eta_{i,\,j}^{i-1/2,\,j} \\
& + (\varphi_{i+1/2,\,j+1/2} - \varphi_{i-1/2,\,j+1/2}) S\xi_{i,\,j}^{i,\,j+1/2} \vec{n}\xi_{i,\,j}^{i,\,j-1/2} \\
& + (\varphi_{i+1/2,\,j-1/2} - \varphi_{i-1/2,\,j-1/2}) S\xi_{i,\,j}^{i,\,j-1/2} \vec{n}\xi_{i,\,j}^{i,\,j-1/2} \big\} \big/ V_{i,\,j}.
\end{aligned} \tag{4.6}$$

This expression has an interpretation in terms of the usual coordinate invariant definition of **grad**

$$\mathbf{grad}\, \varphi = \lim_{V \to 0} \frac{\oint_{\partial V} \varphi \vec{n}\, dS}{V}. \tag{4.7}$$

Consider the "momentum control volume" associated with a node that is defined by pieces of the midcircles as shown in Fig. 5. Let us now consider the piece of the boundary integral that is associated with cell $(i+1/2,\ j+1/2)$, i.e., with the curves $(i+1/2,\ j) - (i+1/2,\ j+1/2)$ and $(i+1/2,\ j+1/2) - (i,\ j+1/2)$. If we assume φ is constant within a cell, equal to $\varphi_{i+1/2,\,j+1/2}$ (as would be true for discrete pressure), then

$$\begin{aligned}
& \int_{(i+1/2,\,j)-(i+1/2,\,j+1/2)} \varphi \vec{n}\, dS + \int_{(i+1/2,\,j+1/2)-(i,\,j+1/2)} \varphi \vec{n}\, dS \\
& \quad = \varphi_{i+1/2,\,j+1/2} \left(\int_{(i+1/2,\,j)-(i+1/2,\,j+1/2)} \vec{n}\, dS + \int_{(i+1/2,\,j+1/2)-(i,\,j+1/2)} \vec{n}\, dS \right).
\end{aligned} \tag{4.8}$$

Now the integral $\oint \vec{n}\, dS$ over any closed contour is zero; therefore in Cartesian coordinates

we can write

$$\left(\int_{(i+1/2,\,j)-(i+1/2,\,j+1/2)} \vec{n}\, dS + \int_{(i+1/2,\,j+1/2)-(i,\,j+1/2)} \vec{n}\, dS \right)$$
$$= -\left(\int_{(i,\,j+1/2)-(i,\,j)} \vec{n}\, dS + \int_{(i,\,j)-(i+1/2,\,j)} \vec{n}\, dS \right). \tag{4.9}$$

If we approximate each of the integrals in the right-hand side of this equation by taking the normal in the corresponding vertex of the original grid multiplied by the area of the subside, we obtain the expression (4.6) for **GRAD**.

The last step breaks the conservation of momentum in the discrete model. For a general discussion relating to preservation of symmetry leading to the loss of conservation of momentum see [3].

5. THE FINITE DIFFERENCE SCHEME

The equations of Lagrangian gas dynamics can be written

$$\frac{d\rho}{dt} = -\rho\, \mathbf{div}\, \vec{U}, \tag{5.1}$$

$$\rho \frac{d\vec{U}}{dt} = -\mathbf{grad}\, p \tag{5.2}$$

$$p \frac{d\varepsilon}{dt} = -p\, \mathbf{div}\, \vec{U}, \tag{5.3}$$

where ρ is the density, p is the pressure, ε is the specific internal energy, and $\vec{U}$ is the velocity.

In this section we describe the discretization of these equations on the new curvilinear grid, using the discrete operators derived in the previous section. We consider the case of a staggered mesh, where the velocity vector is defined on the nodes of the original grid, and all other variables are defined at the "centers" of the cells.

In Lagrangian gas dynamics the nodes move with the local fluid velocity, and the mass of a cell is assumed to be constant in time. We will also assume that the masses of the subcells are constant in time [4]; this implies that the masses of the nodes (i.e., the masses of the figures shown in Fig. (5)) are also constant in time. The mass of a subcell is

$$m_{i,j}^{i+1/2,\,j+1/2} = \rho_{i+1/2,\,j+1/2} V_{i,j}^{i+1/2,\,j+1/2}. \tag{5.4}$$

The mass of a cell and the mass of a node are given by

$$m_{i+1/2,\,j+1/2} = \rho_{i+1/2,\,j+1/2} V_{i+1/2,\,j+1/2}, \tag{5.5}$$

$$m_{i,j} = m_{i,j}^{i+1/2,\,j+1/2} + m_{i,j}^{i-1/2,\,j+1/2} + m_{i,j}^{i-1/2,\,j-1/2} + m_{i,j}^{i+1/2,\,j-1/2}. \tag{5.6}$$

The role of the continuity equation in Lagrangian gas dynamics is played by the diagnostic equation

$$\rho_{i+1/2,\,j+1/2} = \frac{m_{i+1/2,\,j+1/2}}{V_{i+1/2,\,j+1/2}}, \tag{5.7}$$

which relates the density in the cell to the volume. The volume in turn is a known function of the coordinates of the nodes.

The discretizations of the momentum and energy equations are

$$m_{i,j}\frac{\vec{U}_{i,j}^{n+1}-\vec{U}_{i,j}^{n}}{\Delta t}=-V_{i,j}(\mathbf{GRAD}\ p)_{i,j} \tag{5.8}$$

$$m_{i+1/2,j+1/2}\frac{\varepsilon_{i+1/2,j+1/2}^{n+1}-\varepsilon_{i+1/2,j+1/2}^{n}}{\Delta t} = -p_{i+1/2,j+1/2}V_{i+1/2,j+1/2}\left(\mathbf{DIV}\,\frac{\vec{U}^{n+1}+\vec{U}^{n}}{2}\right)_{i+1/2,j+1/2}, \tag{5.9}$$

where the discrete operators **GRAD** and **DIV** have been defined in the previous section.

It is convenient to write these equations in a form similar to the differential case,

$$\rho_{i,j}\frac{\vec{U}_{i,j}^{n+1}-\vec{U}_{i,j}^{n}}{\Delta t}=-(\mathbf{GRAD}\ p)_{i,j} \tag{5.10}$$

$$\rho_{i+1/2,j+1/2}\frac{\varepsilon_{i+1/2,j+1/2}^{n+1}-\varepsilon_{i+1/2,j+1/2}^{n}}{\Delta t}=-p_{i+1/2,j+1/2}\left(\mathbf{DIV}\,\frac{\vec{U}^{n+1}+\vec{U}^{n}}{2}\right)_{i+1/2,j+1/2}, \tag{5.11}$$

where the nodal density $\rho_{i,j}$ is

$$\begin{aligned}\rho_{i,j}=\frac{m_{i,j}}{V_{i,j}} = \{&\rho_{i+1/2,j+1/2}V_{i,j}^{i+1/2,j+1/2}+\rho_{i-1/2,j+1/2}V_{i,j}^{i-1/2,j+1/2}\\ &+\rho_{i-1/2,j-1/2}V_{i,j}^{i-1/2,j-1/2}+\rho_{i+1/2,j-1/2}V_{i,j}^{i+1/2,j-1/2}\}/\{V_{i,j}^{i+1/2,j+1/2}\\ &+V_{i,j}^{i-1/2,j+1/2}+V_{i,j}^{i-1/2,j-1/2}+V_{i,j}^{i+1/2,j-1/2}\}.\end{aligned}$$

To simulate high-speed flows with shocks, we need to introduce artificial viscosity. In Appendix B, we describe the modifications to an edge viscosity introduced in [5] on the new curvilinear grid.

6. PROOF OF SYMMETRY PRESERVATION

6.1. Statement of Symmetry

We will consider the finite difference algorithm in cylindrical coordinates (r, z, ϕ), when there is no dependence on ϕ. Plane, cylindrical, and spherical symmetries can all be considered in this framework. We will prove the symmetry for the finite difference algorithm neglecting the viscous terms. The viscous terms can be analyzed in a similar way.

A statement of the initial and boundary conditions for problems with plane symmetry is as follows. We consider a rectangular domain in r, z coordinates, $(0 \le r \le r_{max}) \times (z_{min} \le z \le z_{max})$; when rotated about the axis of symmetry, the domain becomes a cylinder in 3-D. The component of velocity $u = U_r$ is always equal to zero at $r = 0$ and is set equal to zero at $r = r_{max}$. At $z = z_{min}$ and $z = z_{max}$ we specify either the pressure or the normal component of velocity, $v = U_z$, which do not depend on r but may depend on time. The initial distributions

of the physical parameters are chosen to depend only on z and $U_r = 0$. For such initial and boundary conditions, the solution of the equations of gas dynamics will depend only on z at any later time.

A statement of the initial and boundary conditions for problems with cylindrical symmetry is as follows. We consider the same computational domain as for plane symmetry. The component of velocity $u = U_r$ must still equal zero at $r = 0$; however, at $r = r_{max}$, we specify either $u = U_r$ or the pressure, which may depend on time but does not depend on z. At $z = z_{min}$ and $z = z_{max}$, the normal component of velocity, $v = U_z$, is set to zero. The initial distributions of the physical parameters are chosen to depend only on r, and $U_z = 0$. For such initial and boundary conditions, the solution of the equations of gas dynamics will depend only on r at any later time.

Finally, a statement of the initial and boundary conditions for problems with spherical symmetry is as follows. We consider a domain that is one quarter of a circle in the $r - z$ plane. Then the boundaries of this domain are the straight lines $z = 0$ and $r = 0$ and the circle $r^2 + z^2 = R^2_{max}$; after revolution about the axis of symmetry, the domain is a hemisphere in 3-D. At $r = 0$ the normal component of velocity must be zero, $u = U_r = 0$, and similarly at $z = 0$, we set $v = U_z = 0$. On the circular boundary we can specify either the pressure, which must depend only on the spherical radius, $R = \sqrt{r^2 + z^2}$, or we can specify the normal (spherical) component of the velocity. In either case, the specified function may vary in time; however, at any particular time, the specified function must be constant on the circular boundary. The initial distribution of the physical parameters are chosen to depend only on R. For such initial and boundary conditions, the solution of the equations of gas dynamics will depend only on R at any later time.

In the discrete case, any spatial symmetry can be preserved exactly only on special types of grids. For problems with plane or cylindrical symmetry, the special grid is rectangular, where the nodes $P_{i,j}$ have the coordinates (r_i, z_j), Fig. 6a. For problems with spherical symmetry the special grid is polar, where the nodes $P_{i,j}$ have the coordinates

$$r_{i,j} = R_j \sin\theta_i, \qquad z_{i,j} = R_j \cos\theta_i,$$

and the angle θ equals 0 at the z axis and increases from the z axis to the r axis where it equals $\pi/2$. The polar grid is presented in Fig. 6b.

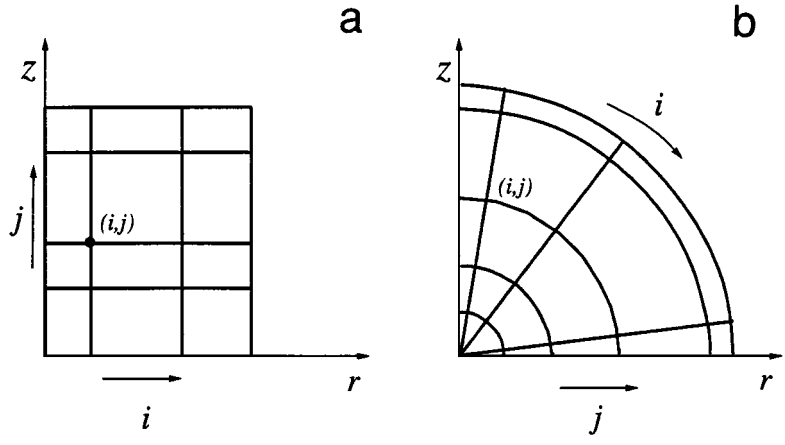

FIG. 6. (a) Grid for plane and cylindrical symmetry, (b) grid for spherical symmetry.

The statement of the initial and boundary conditions for a discrete problem with plane symmetry is as follows. We consider the grid that is shown in Fig. 6a. The range of indices is $1 \le i \le M$, $1 \le j \le N$. The boundary conditions for u are $u^n_{1,j} = 0$, $u^n_{M,j} = 0$. On the top and bottom boundaries, we can specify the pressure, $p^n_{i+1/2,1} = P_{bottom}(t^n)$, $p^n_{i+1/2,N} = P_{top}(t^n)$, or we can specify the normal component of the velocity, $v^n_{i,1} = v_{bottom}(t^n)$, $v^n_{i,N} = v_{top}(t^n)$. We further specify that the initial distribution of physical parameters does not depend on i and that the radial component of velocity, u, is zero everywhere. That is, $\rho^0_{i+1/2,j+1/2} = \rho^0_{j+1/2}$, $p^0_{i+1/2,j+1/2} = p^0_{j+1/2}$, $\varepsilon^0_{i+1/2,j+1/2} = \varepsilon^0_{j+1/2}$, $u^0_{i,j} = u^0_j$, $v^0_{i,j} = 0$. If for these initial and boundary conditions all the physical fields depend only on j at all later times, then we say that the finite difference scheme preserves plane symmetry.

The statement of the initial and boundary conditions for a discrete problem with cylindrical symmetry is as follows. We again consider the grid that is shown in Fig. 6a. The boundary conditions for the axial component of velocity v are $v^n_{i,1} = 0$, $v^n_{i,N} = 0$. On the left boundary we set $u^n_{1,j} = 0$. On the right boundary, we can either specify the pressure, $p^n_{M,j+1/2} = P_{right}(t^n)$, or we can specify u by $u^n_{M,j} = v_{right}(t^n)$. We further specify that the initial distribution of physical parameters does not depend on j and that the velocity component v is zero. That is, $\rho^0_{i+1/2,j+1/2} = \rho^0_{i+1/2}$, $p^0_{i+1/2,j+1/2} = p^0_{i+1/2}$, $\varepsilon^0_{i+1/2,j+1/2} = \varepsilon^0_{i+1/2}$, $v^0_{i,j} = v^0 j$, $u^0_{i,j} = 0$. If for these initial and boundary conditions all the physical fields depend only on i at all later times, then we say that the finite difference scheme preserves cylindrical symmetry.

Lastly, the statement of the initial and boundary conditions for a discrete problem with spherical symmetry is as follows. We consider the grid that is shown in Fig. 6b. The range of the indices is $1 \le i \le M$, $1 \le j \le N$. The boundary condition for u on the r axis is $u^n_{1,j} = 0$. The boundary condition for v on the z axis is $v^n_{M,j} = 0$. At the origin of coordinates, we set $u^n_{1,1} = v^n_{1,1} = 0$. On the circular boundary we can either specify the pressure, $p^n_{i+1/2,N} = P_{top}(t^n)$, or we can specify the normal component of velocity, $u^n_{i,N} \sin\theta_i + v^n_{i,N} \cos\theta_i = U_R(t^n)$, where $U_R(t^n)$ is a given function. We also specify that the initial distributions of density, pressure, and internal energy do not depend on i. That is, $\rho^0_{i+1/2,j+1/2} = \rho^0_{j+1/2}$, $p^0_{i+1/2,j+1/2} = p^0_{j+1/2}$, $\varepsilon^0_{i+1/2,j+1/2} = \varepsilon^0_{j+1/2}$. The initial distribution of velocities is spherical; that is, $u^0_{i,j} = (U_R)^0_j \sin\theta_i$ and $v^0_{i,j} = (U_R)^0_j \cos\theta_i$. If for these initial and boundary conditions, the density, internal energy, and pressure depend only on j and the velocity is spherical—that is, $u^n_{i,j} = (U_R)^n_j \sin\theta_i$ and $v^n_{i,j} = (U_R)^n_j \cos\theta_i$ at all later times—then we say that the finite difference scheme preserves spherical symmetry.

6.2. Areas and Volumes on Rectangular and Polar Grids

The discrete operators and viscous forces are formulated in terms of the areas of the faces and the volumes of the cells. To prove that our finite difference scheme preserves plane, cylindrical, and spherical symmetries, we need to evaluate these formulas for the areas and volumes of the rectangular and the polar grids described in the previous section. In Fig. 7 we show a cell of the rectangular grid and a cell of the polar grid.

For the rectangular grid, the $S\xi$ faces correspond to a fixed value of r (i.e., a constant index i) and the $S\eta$ faces correspond to a fixed value of z (i.e., a constant index j). The expressions for the areas of the left and bottom faces in Fig. 7a are

$$S\xi_{rect} = r_1(z_2 - z_1), \tag{6.1}$$

$$S\eta_{rect} = \frac{r_2 + r_1}{2}(r_2 - r_1). \tag{6.2}$$

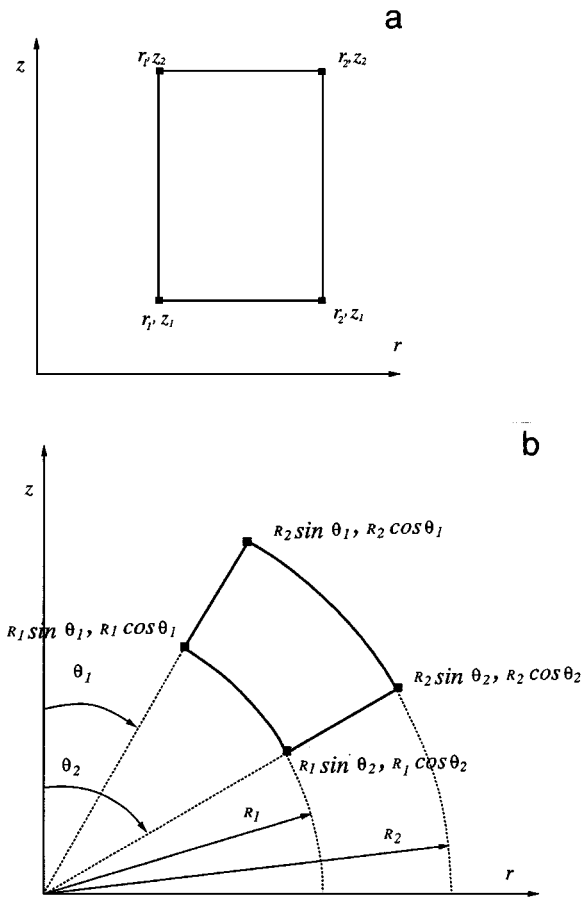

FIG. 7. Cells for the rectangular and polar grids.

The volume of the rectangular cell is

$$V_{rect} = \left(\frac{r_2^2}{2} - \frac{r_1^2}{2}\right)(z_2 - z_1) = \frac{r_2 + r_1}{2}(r_2 - r_1)(z_2 - z_1). \tag{6.3}$$

For the polar grid, the faces $S\xi$ correspond to a fixed value of the angle θ (i.e., a constant index i), and the faces $S\eta$ correspond to a fixed value of the spherical radius (i.e., a constant index j). The expressions for the areas of the faces and the volume of the cell are

$$\begin{aligned} S\xi_{polar} &= \frac{R_2 + R_1}{2}\sin\theta_1(R_2 - R_1), \\ S\eta_{polar} &= R_1^2(\cos\theta_1 - \cos\theta_2), \\ V_{polar} &= \left(\frac{R_2^3}{3} - \frac{R_1^3}{3}\right)(\cos\theta_1 - \cos\theta_2) \\ &= \frac{R_2^2 + R_2R_1 + R_1^2}{3}(R_2 - R_1)(\cos\theta_1 - \cos\theta_2). \end{aligned} \tag{6.4}$$

6.3. The Case of Plane Symmetry

6.3.1. *Symmetry Preservation in the Momentum Equation*

We begin by considering the momentum equation, (5.10), in the case of plane symmetry. We first prove that the nodal density depends only on j. We note that the density of the cells depends only on j and therefore

$$\rho_{i,j} = \{\rho_{j+1/2}(V_{i,j}^{i+1/2,j+1/2} + V_{i,j}^{i-1/2,j+1/2}) + \rho_{j-1/2}(V_{i,j}^{i-1/2,j-1/2} + V_{i,j}^{i+1/2,j-1/2})\}/V_{i,j}.$$

If we introduce the notation

$$r_{i+1/2} = \frac{r_{i+1} + r_i}{2}, \qquad z_{j+1/2} = \frac{z_{j+1} + z_j}{2}, \tag{6.5}$$

then the volumes contained in the expression for $\rho_{i,j}$ are

$$V_{i,j}^{i+1/2,j+1/2} + V_{i,j}^{i-1/2,j+1/2} = \frac{r_{i+1/2} + r_{i-1/2}}{2}(r_{i+1/2} - r_{i-1/2})(z_{j+1/2} - z_j), \tag{6.6}$$

$$V_{i,j}^{i-1/2,j-1/2} + V_{i,j}^{i+1/2,j-1/2} = \frac{r_{i+1/2} + r_{i-1/2}}{2}(r_{i+1/2} - r_{i-1/2})(z_j - z_{j-1/2}), \tag{6.7}$$

$$V_{i,j} = \frac{r_{i+1/2} + r_{i-1/2}}{2}(r_{i+1/2} - r_{i-1/2})(z_{j+1/2} - z_{j-1/2}). \tag{6.8}$$

Therefore

$$\rho_{i,j} = \rho_j = [\rho_{j+1/2}(z_{j+1/2} - z_j) + \rho_{j-1/2}(z_j - z_{j-1/2})]/(z_{j+1/2} - z_{j-1/2}), \tag{6.9}$$

and so the nodal densities also depend only on j.

We next consider the term **GRAD** p in the right-hand side of the momentum equation for the "plane symmetric" pressure field, $p_{i+1/2,j+1/2} = p_{j+1/2}$. In this case,

$$(\mathbf{GRAD}\ p)_{i,j} = (p_{j+1/2} - p_{j-1/2})\frac{(S\eta_{i,j}^{i+1/2,j}\vec{n\eta}_{i,j}^{i+1/2,j} + S\eta_{i,j}^{i-1/2,j}\vec{n\eta}_{i,j}^{i-1/2,j})}{V_{i,j}}.$$

Recognizing that

$$\vec{n\eta}_{i,j}^{i+1/2,j} = \vec{n\eta}_{i,j}^{i-1/2,j} = (0, 1), \tag{6.10}$$

we derive

$$\begin{aligned}(\mathbf{GRAD}_r\ p)_{i,j} &= 0,\\ (\mathbf{GRAD}_z\ p)_{i,j} &= (p_{j+1/2} - p_{j-1/2})\frac{S\eta_{i,j}^{i+1/2,j} + S\eta_{i,j}^{i-1/2,j}}{V_{i,j}}.\end{aligned} \tag{6.11}$$

Using expression (6.8) for $V_{i,j}$ and the following formulas for the areas

$$S\eta_{i,j}^{i+1/2,j} = (r_{i+1/2} + r_i)(r_{i+1/2} - r_i) \tag{6.12}$$

$$S\eta_{i,j}^{i-1/2,j} = (r_i + r_{i-1/2})(r_i - r_{i-1/2}), \tag{6.13}$$

$$S\eta_{i,j}^{i+1/2,j} + S\eta_{i,j}^{i-1/2,j} = \frac{r_{i+1/2} + r_{i-1/2}}{2}(r_{i+1/2} - r_{i-1/2}), \tag{6.14}$$

we finally derive that

$$(\mathbf{GRAD}_z\ p)_{i,j} = (\mathbf{GRAD}_z\ p)_j = \frac{p_{j+1/2} - p_{j-1/2}}{z_{j+1/2} - z_{j-1/2}}. \tag{6.15}$$

That is, the pressure gradient term in the momentum equation is plane symmetric. Thus, when the initial velocity is plane symmetric, the momentum equation produces a plane symmetric velocity field on the next time step.

6.3.2. *The Energy Equation*

We now consider how **DIV** acts on a plane symmetric velocity field, $\vec{U}_{i,j} = (0, v_j)$. Taking into account that one component of velocity is zero, that the normals are parallel to the coordinate axis, and that $S\eta_{i,j}^{i+1/2,j} = S\eta_i^{i+1/2}$, we can show that

$$\begin{aligned}(\mathbf{DIV}\,\vec{U})_{i+1/2,j+1/2} &= (v_{j+1} - v_j)\frac{S\eta_i^{i+1/2} + S\eta_{i+1}^{i+1/2}}{V_{i+1/2,j+1/2}} \\ &= (v_{j+1} - v_j)\frac{0.5(r_{i+1} + r_i)(r_{i+1} - r_i)}{0.5(r_{i+1} + r_i)(r_{i+1} - r_i)(z_{j+1} - z_j)} = \frac{v_{j+1} - v_j}{z_{j+1} - z_j}.\end{aligned} \tag{6.16}$$

That is, $(\mathbf{DIV}\,\vec{U})_{i+1/2,j+1/2} = (\mathbf{DIV}\,\vec{U})_{j+1/2}$ and so the energy equation also will maintain the plane symmetry of the internal energy.

6.4. The Case of Cylindrical Symmetry

6.4.1. *The Momentum Equation*

In the case of cylindrical symmetry, $p_{i+1/2,j+1/2} = p_{i+1/2}$, and so considerations similar to the case of plane symmetry yield the formulas

$$(\mathbf{GRAD}_z\ p)_{i,j} = 0, \tag{6.17}$$

$$(\mathbf{GRAD}_r\ p)_{i,j} = (p_{i+1/2} - p_{i-1/2})\frac{S\xi_{i,j}^{i,j+1/2} + S\xi_{i,j}^{i,j-1/2}}{V_{i,j}}. \tag{6.18}$$

Taking into account that

$$S\xi_{i,j}^{i,j+1/2} = r_i\frac{z_{j+1} - z_j}{2}, \qquad S\xi_{i,j}^{i,j-1/2} = r_i\frac{z_j - z_{j-1}}{2}, \tag{6.19}$$

we derive

$$\begin{aligned}&(\mathbf{GRAD}_z\ p)_{i,j} = 0, \\ &(\mathbf{GRAD}_r\ p)_{i,j} = (\mathbf{GRAD}_r\ p)_i = \frac{r_i}{0.5(r_{i+1/2} + r_{i-1/2})}\frac{p_{i+1/2} - p_{i-1/2}}{r_{i+1/2} - r_{i-1/2}}.\end{aligned} \tag{6.20}$$

We note that this is an approximation for $\partial p/\partial r$, because the ratio $r_i/(0.5(r_{i+1/2} + r_{i-1/2}))$ tends to unity as we refine the grid.

6.4.2. *The Energy Equation*

In the case of cylindrical symmetry, $\vec{U}_{i,j} = (u_i, 0)$. Simple algebraic manipulation gives

$$(\mathbf{DIV}\,\vec{U})_{i+1/2,j+1/2} = (\mathbf{DIV}\,\vec{U})_{i+1/2} = \frac{1}{r_{i+1/2}} \frac{r_{i+1}u_{i+1} - r_i u_i}{r_{i+1} - r_i}, \tag{6.21}$$

which approximates the expression $\frac{1}{r}\frac{\partial(ru)}{\partial r}$ for the divergence of a cylindrically symmetric vector $(u, 0)$ in the continuous case.

6.5. The Case of Spherical Symmetry

6.5.1. *The Momentum Equation*

We now consider the polar grid. In case of spherical symmetry, $p_{i+1/2,j+1/2} = p_{j+1/2}$, and also

$$\vec{n\eta}_{i,j}^{\,i+1/2,j} = \vec{n\eta}_{i,j}^{\,i-1/2,j} = (\sin\theta_i, \cos\theta_i). \tag{6.22}$$

Thus we have

$$(\mathbf{GRAD}_r\ p)_{i,j} = (p_{j+1/2} - p_{j-1/2}) \frac{S\eta_{i,j}^{i+1/2,j} + S\eta_{i,j}^{i-1/2,j}}{V_{i,j}} \sin\theta_i, \tag{6.23}$$

$$(\mathbf{GRAD}_z\ p)_{i,j} = (p_{j+1/2} - p_{j-1/2}) \frac{S\eta_{i,j}^{i+1/2,j} + S\eta_{i,j}^{i-1/2,j}}{V_{i,j}} \cos\theta_i. \tag{6.24}$$

If we introduce the notation

$$R_{j+1/2} = \frac{R_{j+1} + R_j}{2}, \qquad \theta_{i+1/2} = \frac{\theta_{i+1} + \theta_i}{2} \tag{6.25}$$

then

$$\begin{aligned} S\eta_{i,j}^{i+1/2,j} + S\eta_{i,j}^{i-1/2,j} &= R_j^2(\cos\theta_{i-1/2} - \cos\theta_{i+1/2}) \\ V_{i,j} &= \left(\frac{R_{j+1/2}^3}{3} - \frac{R_{j-1/2}^3}{3}\right)(\cos\theta_{i-1/2} - \cos\theta_{i+1/2}), \end{aligned} \tag{6.26}$$

and the expressions for the components of **GRAD** are

$$(\mathbf{GRAD}_r\ p)_{i,j} = \frac{R_j^2}{\left(R_{j+1/2}^2 + R_{j+1/2}R_{j-1/2} + R_{j-1/2}^2\right)/3} \cdot \frac{p_{j+1/2} - p_{j-1/2}}{0.5(R_{j+1} - R_{j-1})} \sin\theta_i, \tag{6.27}$$

$$(\mathbf{GRAD}_z\ p)_{i,j} = \frac{R_j^2}{\left(R_{j+1/2}^2 + R_{j+1/2}R_{j-1/2} + R_{j-1/2}^2\right)/3} \cdot \frac{p_{j+1/2} - p_{j-1/2}}{0.5(R_{j+1} - R_{j-1})} \cos\theta_i. \tag{6.28}$$

It is clear that the gradient is radial in direction and has a magnitude equal to

$$\frac{R_j^2}{\left(R_{j+1/2}^2 + R_{j+1/2}R_{j-1/2} + R_{j-1/2}^2\right)/3} \cdot \frac{p_{j+1/2} - p_{j-1/2}}{0.5(R_{j+1} - R_{j-1})} \tag{6.29}$$

which does not depend on i. This expression approximates the R-component of the gradient in a spherical coordinate system, $\partial p/\partial R$; in the similar fashion to the case of cylindrical symmetry, the factor $R_j^2/((R_{j+1/2}^2 + R_{j+1/2}R_{j-1/2} + R_{j-1/2}^2)/3)$ tends to one as we refine the grid.

6.5.2. *The Energy Equation*

In the case of spherical symmetry, the velocity vector has the form $\vec{U}_{i,j} = (U_j^R \sin\theta_i, U_j^R \cos\theta_i)$, where U^R is the magnitude of the spherical velocity. Taking into account that the velocity vector is orthogonal to the $\vec{n\xi}$ vector at every node, and is parallel to the $\vec{n\eta}$ vector, we have

$$(\mathbf{DIV}\,\vec{U})_{i+1/2,j+1/2} = \frac{U_{j+1}^R\left(S\eta_{i+1/2,j+1}^{i,j+1} + S\eta_{i+1/2,j+1}^{i+1,j+1}\right) - U_j^R\left(S\eta_{i+1/2,j}^{i,j} + S\eta_{i+1/2,j}^{i+1,j}\right)}{V_{i+1/2,j+1/2}}. \tag{6.30}$$

Using the formulas for areas and volumes, we derive

$$(\mathbf{DIV}\,\vec{U})_{i+1/2,j+1/2} = (\mathbf{DIV}\,\vec{U})_{j+1/2} = \frac{1}{\left(R_{j+1}^2 + R_{j+1}R_j + R_j^2\right)/3}\,\frac{R_{j+1}^2 U_{j+1}^R - R_j^2 U_j^R}{R_{j+1} - R_j}, \tag{6.31}$$

which approximates the divergence of a spherically symmetric vector field $-(1/R^2)(\partial(R^2U^R)/\partial R)$.

7. VIOLATION OF SPHERICAL SYMMETRY FOR THE CONVENTIONAL SCHEME

Here we show analytically that the scheme (5.10), (5.11), which uses the grid with straight lines, does not preserve spherical symmetry. A numerical example demonstrating this phenomenon will be presented in the next section.

For polar distributions of nodes, the grid with straight lines in shown in Fig. 3b. The formulas (4.2), (4.6) for discrete divergence and gradient remain valid for this grid. Moreover, in this case the normals corresponding to one side are the same, for example, $\vec{n\xi}_{i+1,j}^{i+1,j+1/2} = \vec{n\xi}_{i+1,j+1}^{i+1,j+1/2}$. However, Eq. (6.22) is not valid anymore, and instead we have

$$\vec{n\eta}_{i,j}^{i+1/2,j} = (\sin\theta_{i+1/2}, \cos\theta_{i+1/2}), \qquad \vec{n\eta}_{i,j}^{i-1/2,j} = (\sin\theta_{i-1/2}, \cos\theta_{i-1/2}). \tag{7.1}$$

The formulas (6.23) now take the form

$$(\mathbf{GRAD}_r\, p)_{i,j} = (p_{j+1/2} - p_{j-1/2})\frac{S\eta_{i,j}^{i+1/2,j}\sin\theta_{i+1/2} + S\eta_{i,j}^{i-1/2,j}\sin\theta_{i-1/2}}{V_{i,j}}, \tag{7.2}$$

$$(\mathbf{GRAD}_z\, p)_{i,j} = (p_{j+1/2} - p_{j-1/2})\frac{S\eta_{i,j}^{i+1/2,j}\cos\theta_{i+1/2} + S\eta_{i,j}^{i-1/2,j}\cos\theta_{i-1/2}}{V_{i,j}}. \tag{7.3}$$

Let us consider the simplest case of a uniform-in-angle polar grid. Then after some algebra, one can transform these equations to a form similar to (6.27), (6.28), where instead of $\sin\theta_i$

and $\cos\theta_i$ we will have following approximations to these quantities

$$2 \cdot \frac{\sin^2\theta_{i-1/2} + 2\sin^2\theta_i + \sin^2\theta_{i+1/2}}{\sin\theta_{i-1} + 6\sin\theta_i + \sin\theta_{i+1}}, \tag{7.4}$$

$$2 \cdot \frac{\cos\theta_{i-1/2}\sin\theta_{i-1/2} + 2\cos\theta_i\sin\theta_i + \cos\theta_{i+1/2}\sin\theta_{i+1/2}}{\sin\theta_{i-1} + 6\sin\theta_i + \sin\theta_{i+1}}. \tag{7.5}$$

These expressions clearly depend not only on the angle θ_i but also on the angles θ_{i-1} and θ_{i+1}; the gradient is not in the radial direction and therefore spherical symmetry is violated.

8. NUMERICAL EXAMPLES

In this section we present two examples using the curvilinear grid, both in cylindrical coordinates. The first example is Noh's spherically divergent infinite shock, for a perfect gas robustness of our new method in a case where the initial grid does not reflect the symmetry of the flow.

8.1. Spherical Noh Problem

Here we consider the spherical Noh problem. The problem domain starts as the unit sphere. The initial state of the fluid is uniform, with a density of one and an internal energy of zero. The initial velocity is directed radially inward with magnitude of -1.0. The fluid obeys an ideal gas equation of state with gas constant $\gamma = 5/3$. Although an analytic solution exists for the time evolution of the spherical Noh problem, here we consider only the symmetry aspect. See [5] for a more detailed description of the problem solution. We begin with the case of a radial grid that is uniform in angle, shown in Fig. 8. At $t = 0.6$ we show the resulting grid from two calculations: one in which we use straight lines to connect the nodes (Fig. 8a), and the other where we use curvilinear elements to reconstruct the grid (Fig. 8b). The curvilinear grid stays spherically symmetric, confirming our theoretical results in Subsection 6.5. The grid based on linear segments becomes highly distorted near the shock front, which eventually causes the calculation to stop.

Next we rerun the spherical Noh problem with an initial grid that is nonuniform in angle. Using the standard method based on linear grid reconstruction, this problem will not run up

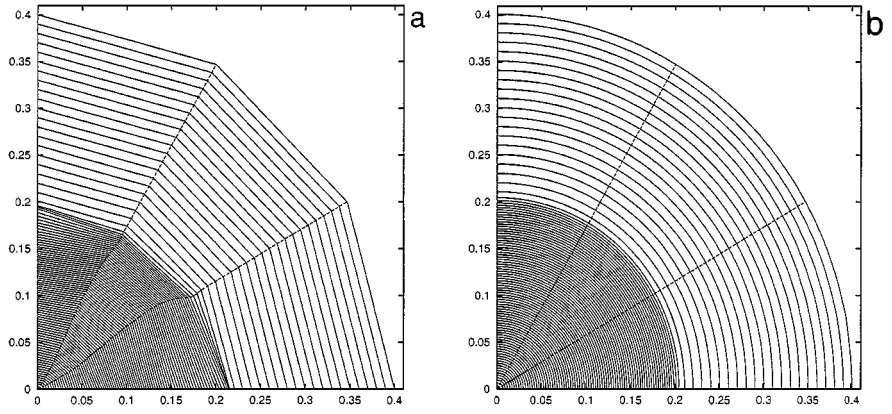

FIG. 8. A uniform-in-angle grid for Noh's problem; (a) conventional scheme, (b) new scheme.

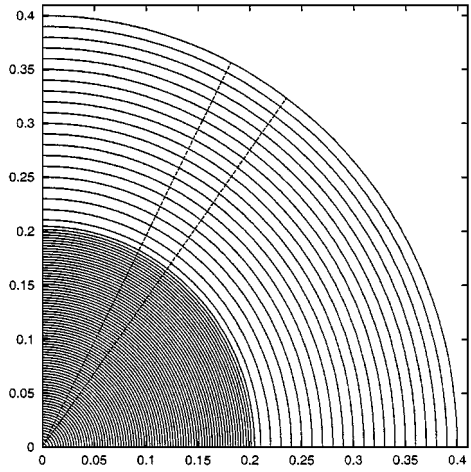

FIG. 9. A nonuniform-in-angle grid for Noh's problem.

to $t = 0.6$ because of the severe grid distortion. The grid for the new method is presented in Fig. 9. Again this grid remains perfectly symmetric, as predicted by our theory.

8.2. Saltzman's Problem

Here we present results for the well-known Saltzman piston problem. This problem tests the ability of a code to maintain a one-dimensional solution to a one-dimensional problem when run on a nonuniform two-dimensional mesh. The problem domain consists of a cylinder whose lateral surface and bottom base are free-slip stationary walls, while the top is a piston moving with a constant downward velocity that drives a strong shock into the fluid. The analytic solution of this problem is one dimensional, depending only on the axial coordinate z, and in our terminology has plane symmetry. In the numerical simulation, however, the one-dimensional flow symmetry is broken by the computational mesh. The initial mesh contains 10 cells in the r direction and 100 cells in the z direction and is defined by

$$r_{i,j} = (j-1)h_r, \tag{8.1}$$

$$z_{i,j} = 1 - (i-1) * h_z + (11-j)h_r \sin\frac{\pi(i-1)}{100} \tag{8.2}$$

$$i = 1, 2, \ldots, 101; \qquad j = 1, 2, \ldots, 11, \tag{8.3}$$

where $h_r = h_z = 0.01$. The grid is shown in Fig. 10.

The fluid is assumed to be an ideal gas with gas constant $\gamma = 5/3$. The piston moves downward with a constant velocity of 1. The fluid is initially at rest, with a density of one and with internal energy 10^{-4}. The analytic post shock conditions are described by a pressure of 1.333, a density of 4, and an internal energy of 0.5; the shock speed is 1.333.

Our aim in choosing this problem is to demonstrate the robustness of our new method. It is well known that the initial nonuniform grid leads to mesh tangling, because of the presence of an "hourglass" mode and of artificial vorticity [11, 14]. We do not expect the curvilinear grid to significantly improve our solution; rather we will demonstrate that the simulation on the new grid will not be noticeably worse.

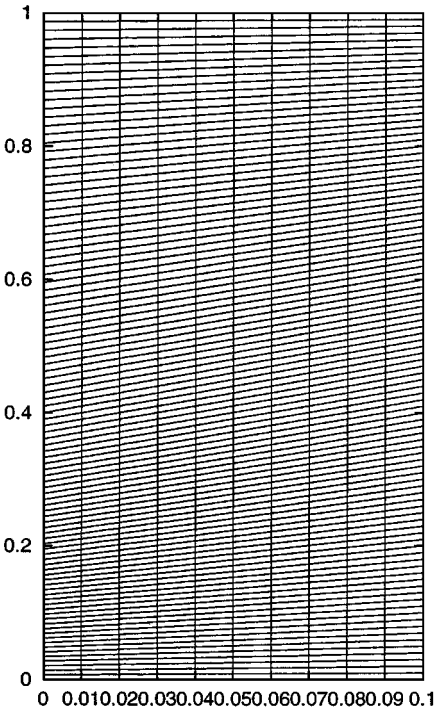

FIG. 10. Initial grid for Saltzman's problem.

Because the initial grid consists of straight lines, all the initial conditions including the distribution of masses are the same for the standard and for the new methods. Furthermore, because the initial grid is not rectangular, the new method will not preserve the planar symmetry. In Fig. 11 we present the grids for the standard method (a), and new method (b)

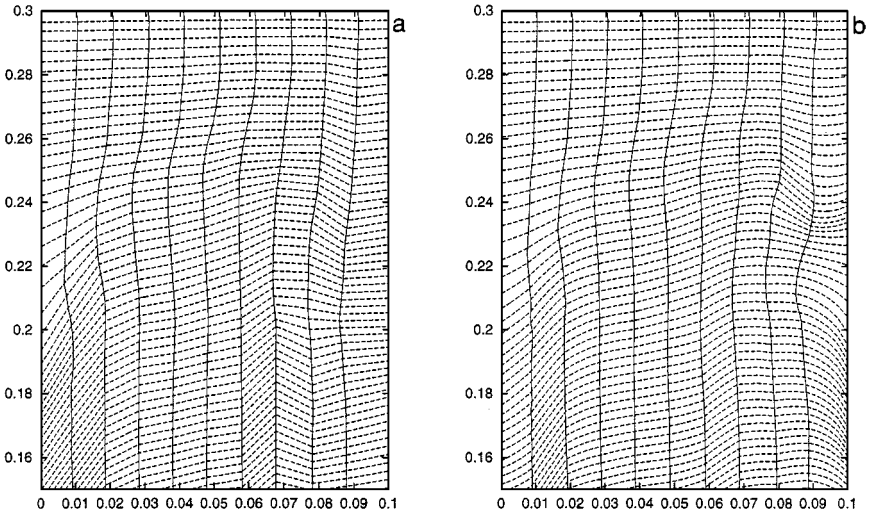

FIG. 11. Grids for the Saltzman piston problem; (a) conventional scheme, (b) new scheme.

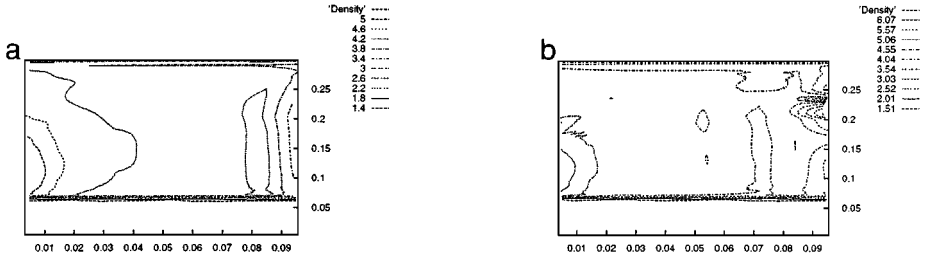

FIG. 12. Isolines of density for the Saltzman piston problem; (a) conventional scheme, (b) new scheme.

(we present only the portions of the grid where the most severe tangling occurs). The grid for the new method looks very reasonable when compared with the standard method and is perhaps even smoother in the interior. Near the right boundary we can see cells with clearly curvilinear sides. It appears that this is an artificial phenomenon, the result of insufficient resolution near this boundary. To show how the grid influences the density field we compare the isolines of density for the two methods in Fig. 12. The resolution of the shock front is almost the same in the two calculations. The new method gives better results near the z axis, while the standard method gives better results near the right boundary. We note that the artificially curved cells near the right boundary lead to some overcompression. We consider these results to be very satisfactory. On the other hand, it is also clear that for practical applications we will need some modification of our grid reconstruction algorithm, to include limiters that control how big the change in angle can be for any side of the cell.

9. CONCLUSION

It is clear that there are still many issues that need to be addressed. For example, one important issue will be to improve the robustness of the grid reconstruction algorithms. It is possible to reconstruct the grid to ensure that the tangent vector to the grid lines will be continuous at the grid points (which is not the case for the grid reconstruction procedure described in this paper). There are many ways to do this. Also, one can use a linear blending of the local circles, or use cubic Hermite interpolation. The main issue here is to determine which approach is more accurate and robust. A related idea is to introduce limiters that control the variability of the tangent of the reconstructed curve, leading to a smoother grid.

An alternate approach is to develop an equation for the evolution of the curvature of each segment, as opposed to reconstructing the grid at each time step. This approach might be especially useful in simulating the evolution of unstable interfaces, where the mesh ultimately will not be sufficient to resolve the developing small features, but where an appropriate equation can predict these small features by evolving the curvature.

Another important question is how the curvilinear grid affects the accuracy of the simulation. We will investigate this question in the context of elliptic equations, where again we can use the discrete operators constructed in this paper.

In summary, we have demonstrated the feasibility of preserving certain physical symmetries in numerical simulations of fluid flow by using higher-order reconstructions of the computational grid. In particular, we used arcs of the circles to connect the nodes and showed that planar, cylindrical, and spherical symmetries could be maintained exactly. While demonstrating feasibility, we recognize that our particular algorithm is constructed heuristically, and that continued research may lead to further significant improvements.

Nevertheless, we believe that the utility of our more general grid reconstruction is in itself worth illustrating.

APPENDIX A: LENGTHS, AREAS, AND VOLUMES

We start with the 2-D figures. Because the curve that connects two nodes is an arc of a local circle, its length is

$$L = R * |\omega|, \tag{A.1}$$

where R is the radius of the local circle and ω is the central angle.

To compute the area of a quadrilateral with curved sides, we first compute the area of the associated quadrilateral with straight sides (obtained by connecting the nodes by straight lines), and then adding or subtracting the partial areas (segments) enclosed by an arc and the chord formed by the straight line, see Fig. 13. For the area of each segment of the circle, we use the well-known formula

$$S_{segment\ of\ circle} = \frac{R^2}{2} * ((|\omega| - \sin(|\omega|)). \tag{A.2}$$

It is easy to decide whether to add or subtract the area of the segment based on the sign of ω.

Next we consider the 3-D figures of revolution. To compute the areas of the faces of the figures of rotation, we use the formula

$$S = r_c R(\alpha_1 - \alpha_0) + R^2(\sin(\alpha_1) - \sin(\alpha_0)), \tag{A.3}$$

where r_c is the radial coordinate of the center of the local circle, R is the radius of the local circle, and α_0, α_1 are the polar angles corresponding to the endpoints of the arc of the circle. This formula can be easily obtained from the fact that the elementary area is

$$dS = (R\,d\alpha)(r_c + R\cos(\alpha)), \tag{A.4}$$

recognizing that R is constant on the surface.

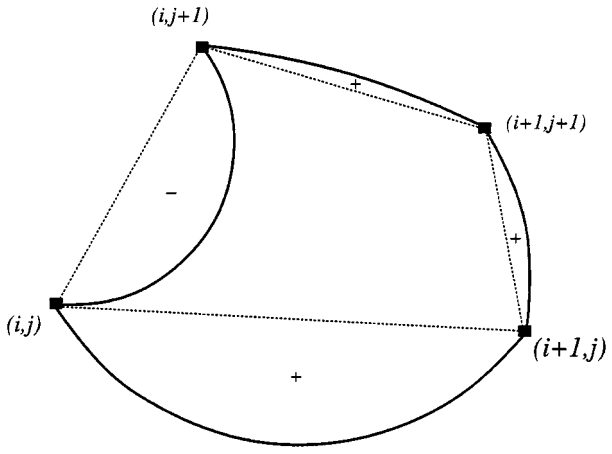

FIG. 13. Illustration of procedure for computation of the area of a curved quadrilateral.

To compute the volume of the figure of revolution, we use a similar logic as that used to compute the areas of the 2-D figures with curved boundaries. First, we calculate the volume of the figure of revolution of the quadrilateral with straight sides and then we add or subtract the volumes of figure of revolution of the segments of the circles. To compute the volume of the quadrilateral with straight sides we subdivide the quadrilateral into two triangles and then compute the individual volumes of these triangles. The volume of the figure of revolution of a triangle is the product of its area with the r_m coordinate of the center of mass. For a triangle r_m is just one third of the sum of the r coordinates of the three vertices of the triangle. The volume of the figure of revolution of the segment of a circle equals

$$V = \frac{R^2}{2} r_c[(\alpha_1 - \alpha_0) - \sin(\alpha_1 - \alpha_0)] + \frac{R^3}{6}[2(\sin(\alpha_1) - \sin(\alpha_0)) - (\cos(\alpha_1) + \cos(\alpha_0))\sin(\alpha_1 - \alpha_0)].$$

This formula is obtained as the difference of the volumes of the figures obtained by rotation of the sector of the circle and the triangle formed by the rays of the circle and the corresponding chord, see Fig. 14. The volume of revolution of the triangle $P_0 O P_1$ is

$$V_{triangle} = \frac{R^2}{2} r_c \sin(\alpha_1 - \alpha_0) + \frac{R^3}{6}(\cos(\alpha_1) + \cos(\alpha_0))\sin(\alpha_1 - \alpha_0). \tag{A.5}$$

The volume of the elementary sector centered at angle α and subtending the angle $d\alpha$ is

$$dV_{sector} = \left(r_c + \frac{2}{3} R\cos(\alpha)\right)\frac{R^2}{2} - d\alpha, \tag{A.6}$$

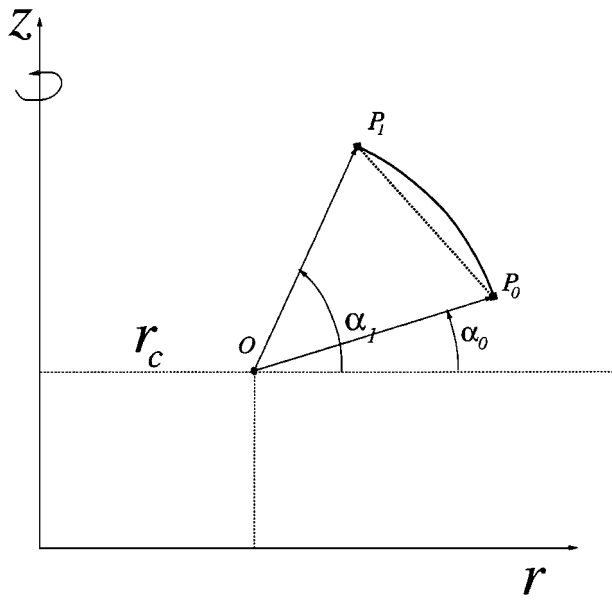

FIG. 14. Illustration for derivation of the formula for the volume of a figure of revolution.

and integration over α gives

$$V_{sector} = \frac{R^2}{2} r_c(\alpha_1 - \alpha_0) + \frac{R^3}{3}[\sin(\alpha_1) - \sin(\alpha_0)], \tag{A.7}$$

and finally,

$$V = V_{sector} - V_{triangle}. \tag{A.8}$$

APPENDIX B: EDGE ARTIFICIAL VISCOSITY

It is necessary to introduce artificial viscosity to simulate high-speed flows with shocks. The purpose of the artificial viscosity is to spread shocks and other steep wave fronts over several grid points. In this section, we describe the modifications to the edge viscosity introduced in [5] necessitated by the new curvilinear grid. We do not give any motivation or derivation for this form of the viscosity, but simply present the computational formulas.

In Fig. 15 we illustrate the additional geometrical elements needed to describe the viscous forces. The artificial viscous forces are associated with the subtriangles that are shown in Fig. 15. In each cell we define four forces related to the four subtriangles. For example, the force related to cell $i+1/2,\ j+1/2$ and to the triangle that includes the edge $i+1/2,\ j$ is

$$\begin{aligned}\vec{f}_{i+1/2,\,j}^{\,i+1/2,\,j+1/2} &= q_{i+1/2,\,j}^{i+1/2,\,j+1/2}(1-\psi_{i+1/2,\,j})S\vec{\xi}_{i+1/2,\,j}^{\,i+1/2,\,j+1/2} \\ &\quad\times \delta\left[\left(\widehat{\Delta\vec{U}}_{i+1/2,\,j}, \vec{n\xi}_{i+1/2,\,j}^{\,i+1/2,\,j+1/2}\right)\right]\widehat{\Delta\vec{U}}_{i+1/2,\,j}.\end{aligned} \tag{B.1}$$

Here the superscripts denote the cell, and the subscripts identify the side of the cell, which uniquely determines the triangle. Also, $q_{i+1/2,\,j}^{i+1/2,\,j+1/2}$ is the scalar part of the viscosity, $\psi_{i+1/2,\,j}$ is a limiter, and δ is a switch used to turn the viscosity on or off. The vector $\vec{n\xi}_{i+1/2,\,j}^{\,i+1/2,\,j+1/2}$ is the unit normal to the circle at the point $i+1/2,\ j$. $S\vec{\xi}_{i+1/2,\,j}^{\,i+1/2,\,j+1/2}$ is the area of the arc

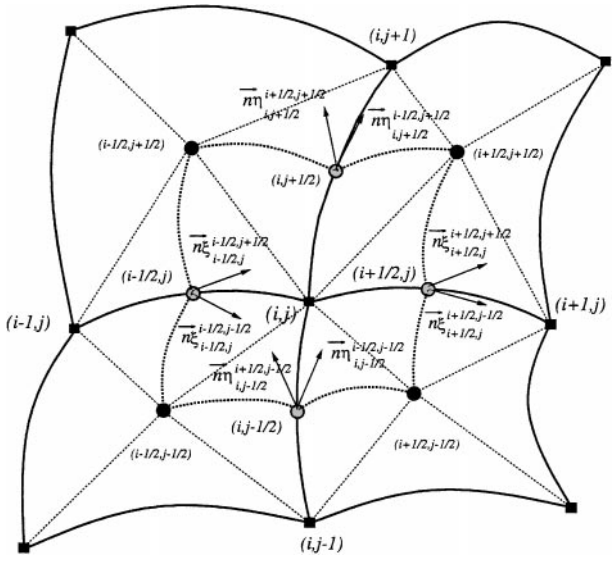

FIG. 15. Geometrical elements involved in the description of the viscous forces.

connecting points $i+1/2,\ j$, and $i+1/2,\ j+1/2$, and $\widehat{\Delta\vec{U}}_{i+1/2,\,j}$ is the unit vector in the direction of $\vec{U}_{i+1/2,\,j}-\vec{U}_{i,\,j}$, that is,

$$\Delta\vec{U}_{i+1/2,\,j}=\vec{U}_{i+1,\,j}-\vec{U}_{i,\,j},\qquad \widehat{\Delta\vec{U}}_{i+1/2,\,j}=\frac{\Delta\vec{U}_{i+1/2,\,j}}{|\Delta\vec{U}_{i+1/2,\,j}|}. \tag{B.2}$$

The scalar part of the viscosity, q, in the case of an ideal gas with gas constant γ, is given by

$$q_{i+1/2,\,j}^{\,i+1/2,\,j+1/2}=\rho_{i+1/2,\,j+1/2}\left\{\frac{\gamma+1}{4}|\Delta\vec{U}_{i+1/2,\,j}|+\sqrt{\left(\frac{\gamma+1}{4}\right)^2(\Delta\vec{U}_{i+1/2,\,j})^2+C_{i+1/2,\,j+1/2}^2}\right\}, \tag{B.3}$$

where $C_{i+1/2,\,j+1/2}$ is the speed of sound in the cell. The limiter ψ is defined as

$$\psi_{i+1/2.\,j}=\max\left\{0,\min\left[\frac{r_{i+1/2,\,j}^l+r_{i+1/2,\,j}^r}{2},2r_{i+1/2,\,j}^l,2r_{i+1/2,\,j}^r,1\right]\right\}, \tag{B.4}$$

where

$$r_{i+1/2,\,j}^l=\frac{\Delta\vec{U}_{i-1/2,\,j}\cdot\widehat{\Delta\vec{U}}_{i+1/2,\,j}}{\Delta\vec{x}_{i-1/2,\,j}\cdot\widehat{\Delta\vec{x}}_{i+1/2,\,j}}\Big/\frac{|\Delta\vec{U}_{i+1/2,\,j}|}{|\Delta\vec{x}_{i+1/2,\,j}|},$$

$$r_{i+1/2,\,j}^r=\frac{\Delta\vec{U}_{i+3/2,\,j}\cdot\widehat{\Delta\vec{U}}_{i+1/2,\,j}}{\Delta\vec{x}_{i+3/2,\,j}\cdot\widehat{\Delta\vec{x}}_{i+1/2,\,j}}\Big/\frac{|\Delta\vec{U}_{i+1/2,\,j}|}{|\Delta\vec{x}_{i+1/2,\,j}|}.$$

In the last two equations, $\Delta\vec{x}$ is defined similarly to $\Delta\vec{U}$, (B.2), where $\vec{x}$ is the coordinate vector. The switch function is defined as

$$\delta[s]=\begin{cases}s, & \text{if } s<0\\ 0, & \text{if } s\geq 0.\end{cases} \tag{B.5}$$

The forces acting on the other triangles in a cell are defined in an analogous manner, making necessary changes to the indices.

The discrete momentum equation, including all the viscous forces that surround the node, can be written as

$$\rho_{i,\,j}\frac{\vec{U}_{i,\,j}^{n+1}-\vec{U}_{i,\,j}^{n}}{\Delta t}=-(\mathbf{GRAD}\ p)_{i,\,j}+\{\vec{f}_{i+1/2,\,j}^{\,i+1/2,\,j+1/2}+\vec{f}_{i,\,j+1/2}^{\,i+1/2,\,j+1/2}+\vec{f}_{i,\,j+1/2}^{\,i-1/2,\,j+1/2}+\vec{f}_{i-1/2,\,j}^{\,i-1/2,\,j+1/2}+\vec{f}_{i-1/2,\,j}^{\,i-1/2,\,j-1/2}+\vec{f}_{i,\,j-1/2}^{\,i-1/2,\,j-1/2}+\vec{f}_{i,\,j-1/2}^{\,i+1/2,\,j-1/2}+\vec{f}_{i+1/2,\,j}^{\,i+1/2,\,j-1/2}\}/V_{i,\,j}.$$

Applying the principle of compatibility [6] the corresponding energy equation is

$$\rho_{i+1/2,\,j+1/2}\frac{\varepsilon^{n+1}_{i+1/2,\,j+1/2}-\varepsilon^{n}_{i+1/2,\,j+1/2}}{\Delta t}$$
$$=-p_{i+1/2,\,j+1/2}\left(\mathbf{DIV}\frac{\vec{U}^{n+1}+\vec{U}^{n}}{2}\right)_{i+1/2,\,j+1/2}+\Big\{\big(\vec{f}^{\,i+1/2,\,j+1/2}_{i+1/2,\,j},\Delta\vec{U}^{n+1/2}_{i+1/2,\,j}\big)$$
$$+\big(\vec{f}^{\,i+1/2,\,j+1/2}_{i,\,j+1/2},\Delta\vec{U}^{n+1/2}_{i,\,j+1/2}\big)+\big(\vec{f}^{\,i+1/2,\,j+1/2}_{i+1,\,j+1/2},\Delta\vec{U}^{n+1/2}_{i+1,\,j+1/2}\big)$$
$$+\big(\vec{f}^{\,i+1/2,\,j+1/2}_{i+1/2,\,j+1},\Delta\vec{U}^{n+1/2}_{i+1/2,\,j+1}\big)\Big\}\big/V_{i+1/2,\,j+1/2}. \tag{B.6}$$

The superscript $n+1/2$ indicates that this term is computed using the arithmetic mean of the old and new velocities.

ACKNOWLEDGMENTS

This work was performed under the auspices of the U.S. Department of Energy under Contract W-7405-ENG-36 and DOE/BES Program in the Applied Mathematical Sciences Contract KC-07-01-01. The authors also acknowledge the support of DOE's Accelerated Strategic Computing Initiative (ASCI). The authors thank E. Caramana, J. Hyman, R. Liska, B. Swartz, P. Whalen, and J. Morel for many fruitful discussions and constructive comments on various drafts of this paper.

REFERENCES

1. O. M. Belotserkovskii, V. V. Demchenko, V. I. Kosarev, and A. S. Kholodov, Numerical simulation of some problems of laser compression of shells, *USSR Comput. Math. Math. Phys.* **18**, 117 (1978).
2. D. J. Benson, Computational methods in Lagrangian and Eulerian hydrocodes, *Comput. Methods Appl. Mech. Engrg.* **99**, 235 (1992).
3. E. J. Caramana and P. P. Whalen, Numerical preservation of symmetry properties of continuum problems, *J. Comput. Phys.* **141**, 174 (1998).
4. E. J. Caramana and M. J. Shashkov, Elimination of artificial grid distortion and hourglass-type motions by means of Lagrangian subzonal masses and pressures, *J. Comput. Phys.* **142**, 521 (1998).
5. E. J. Caramana, M. J. Shashkov, and P. P. Whalen, Formulations of artificial viscosity for multi-dimensional shock wave computations, *J. Comput. Phys.* **144**, 70 (1998).
6. E. J. Caramana, D. E. Burton, M. J. Shashkov, and P. P. Whalen, The construction of compatible hydrodynamics algorithms utilizing conservation of total energy, *J. Comput. Phys.* **146**, 227 (1998).
7. J. Saltzman and P. Colella, *Second-Order Upwind Transport Methods for Lagrangian Hydrodynamics*, Report LA-UR-85-678, Los Alamos National Laboratory, Los Alamos, NM.
8. P. G. Ciarlet and P.-A. Raviart, Interpolation theory over curved elements, with applications to finite element methods, *Comput. Methods Appl. Mech. Engrg.* **1**, 217 (1972).
9. P. G. Ciarlet and P.-A. Raviart, The combined effect of curved boundaries and numerical integration in isoparametric finite element methods, in *The Mathematical Foundations of the Finite Element Method with Applications to Partial Differential Equations*, edited by A. K. Aziz (Academic Press, New York, 1972), pp. 409–475.
10. V. A. Dorodnytsin, Finite difference models entirely inheriting continuous symmetry of original differential equations, *Internat. J. Modern Phys. C* **5**, 723 (1994).
11. J. K. Dukowicz and B. Meltz, Vorticity errors in multidimensional Lagrangian codes, *J. Comput. Phys.* **99**, 115 (1992).
12. M. H. Emery, J. H. Gardner, R. H. Lehmberg, and S. P. Obenschain, Hydrodynamics target response to an induced spatial incoherence-smoothed laser beam, *Phys. Fluids B* **3**, 2640 (1991).

13. R. G. Evans, A. J. Bennet, and G. J. Pert, Rayleigh–Taylor instabilities in laser-accelerated targets, *Phys. Rev. Lett.* **49**, 1639 (1982).
14. J. R. Freeman, M. J. Clauser, and S. L. Thompson, Rayleigh–Taylor instabilities in inertial-confinement fusion targets, *Nuclear Fusion* **17**, 223 (1997).
15. S. K. Godunov, A. V. Zabrodin, and M. Ya. Ivanov, *et al.*, *Numerical Solution of Multidimensional Problems of Gas Dynamics* (Nauka, Moscow, 1976). [In Russian]
16. P. S. Huyakorn and P. F. Andersen, A curvilinear finite element model for simulating two-well tracer tests and transport in stratified aquifer, *Water Resources Res.* **22**, 663 (1986).
17. J. M. Hyman and M. Shashkov, Natural discretizations for the divergence, gradient, and curl on logically rectangular grids, *Internat. J. Comput. Math. Appl.* **33**, 81 (1997).
18. J. M. Hyman and M. Shashkov, The adjoint operators for natural discretizations for the divergence, gradient and curl on logically rectangular grids, *IMACS J. Appl. Numer. Math.* **25**, 413 (1997).
19. J. M. Hyman and M. Shashkov, The orthogonal decomposition theorems for mimetic finite difference methods, *SIAM J. Numer. Anal.*, in press.
20. J. M. Hyman and M. Shashkov, The approximation of boundary conditions for mimetic finite difference methods, *Internat. J. Comput. Math. Appl.* **36**, 79 (1988).
21. P. M. Knupp and S. Steinberg, *The Fundamentals of Grid Generation* (CRC Press, Boca Raton, 1993).
22. V. A. Korobytsin, Invariant variational-difference schemes and conservation laws, *USSR Comput. Math. Math. Phys.* **29**, 71 (1989).
23. A. M. Latypov, Approximate Lie group-analysis of finite-difference equations, *Dynam. Continuous Discrete Impulsive Systems* **3**, 483 (1997).
24. D. Leutloff, K. G. Roesner, and R. C. Srivastava, Numerical investigation of three-dimensional shock focusing effects by invariant difference scheme, *Fluid Dynam. Res.* **10**, 469 (1992).
25. L. Margolin and B. Nichols, Fundamental considerations in the integration of the momentum equations in finite difference codes, in *Proc. of 3rd International Conference on Numerical Methods in Laminar and Turbulent Flow* (University of Washington, 1983).
26. L. G. Margolin and B. D. Nichols, *Momentum Control Volumes for Finite Difference Codes*, Report LA-UR-83-524, Los Alamos National Laboratory, NM, 1983.
27. L. G. Margolin and M. Shashkov, Preserving symmetries in Lagrangian hydro codes, unpublished.
28. W. F. Noh, Errors for calculations of strong shocks using an artificial viscosity and an artificial heat flux, *J. Comput. Phys.* **72**, 72 (1978).
29. M. Shashkov, *Conservative Finite-Difference Methods on General Grids* (CRC Press, Boca Raton, 1995).
30. M. Shashkov and S. Steinberg, Support-operator finite-difference algorithms for general elliptic problems, *J. Comput. Phys.* **118**, 131 (1995).
31. M. Shashkov and S. Steinberg, Solving diffusion equations with rough coefficients in rough grids, *J. Comput. Phys.* **129**, 383 (1996).
32. A. S. Shvedov, A difference scheme for the equation of gas dynamics which conserves the group properties of solutions, *Math. Notes* **48**, 1064 (1990).
33. L. V. Shurshalov, The choice of the initial divergent form of the equations for calculating axisymmetric flows by finite-difference methods, *USSR Comput. Math. Math. Phys.* **20**, 265 (1980).
34. A. Solov'ov, E. Solov'ova, V. Tishkin, A. Favorskii, and M. Shashkov, Dirichlet-particle method difference schemes, conserving the one-dimensionality of gas-dynamics flow in rectangular, cylindrical and spherical coordinates, *Differential Equations* **23**, 1443 (1987).
35. A. Solov'ev and M. Shashkov, Difference scheme for the Dirichlet-particle method in cylindrical coordinates, conserving symmetry of gas-dynamical flow, *Differential Equations* **24**, 817 (1988).
36. P. Silvester and R. Rafinejad, Curvilinear finite elements for two-dimensional saturable magnetic fields, *IEEE Trans. Power Apparatus Systems* **93**, 1861 (1974).
37. R. P. J. Town and A. R. Bell, Three-dimensional simulations of the implosion of inertial confinement fusion targets, *Phys. Rev. Lett.* **67**, 1863 (1991).

38. V. F. Tishkin, N. N. Turina, and A. P. Favorskii, Difference schemes for calculating hydrodynamical flows in cylindrical coordinates, Preprint 23, Institute of Applied Mathematics of Russian Academy of Sciences, Moscow, Russia, 1978. [In Russian]
39. P. P. Volosevich, and E. G. Gamalii, *et al.*, Two-dimensional effects in laser compression of glass shells, *JETP Lett.* **24**, 252 (1976).
40. R. F. Warming and B. J. Hyett, The modified equation approach to the stability and accuracy analysis of finite-difference methods, *J. Comput. Phys.* **14**, 159 (1974).
41. M. Zlamal, The finite element method in domains with curved boundaries, *Internat. J. Numer. Meth. Engrg.* **5**, 367 (1973).
42. M. Zlamal, Curved elements in the finite element method, I, *SIAM J. Numer. Anal.* **10**, 229 (1973).